A&A 366, 651–661 (2001)
DOI: 10.1051/0004-6361:20000258

Astronomy & Astrophysics

H_2 infrared emission and the formation of dense structures in the Orion molecular cloud

L. Vannier[1], J. L. Lemaire[⋆,1,2], D. Field[⋆,3], G. Pineau des Forêts[1], F. P. Pijpers[4], and D. Rouan[1]

[1] Observatoire de Paris-Meudon, 92195 Meudon Principal Cedex, France
[2] Université de Cergy-Pontoise UMR 8588 du CNRS, 95806 Cergy Cedex, France
[3] Institute of Physics and Astronomy, University of Aarhus, 8000 Aarhus C, Denmark
and Observatoire de Paris-Meudon, UMR 8588 du CNRS, France
[4] Theoretical Astrophysics Centre, University of Aarhus, 8000 Aarhus C, Denmark

Received 21 June 2000 / Accepted 9 November 2000

Abstract. Observations are reported of IR emission of H_2 from a region of the Orion molecular cloud (OMC1) between the Becklin-Neugebauer object and IRc2 to the north and the Trapezium stars to the south. Data were obtained using the ESO 3.6 m telescope in the K-band around 2 μm with the ADONIS adaptive optics system. Images of H_2 $v = 1{-}0$ $S(1)$ show a spatial resolution of $\sim$0.15″. Detailed investigations of the distribution of sizes of structures in our images have been performed by area-perimeter analysis, Fourier analysis and brightness distribution studies. These demonstrate that structure is not fractal but shows a preferred scales of between 3 10^{-3} and 4 10^{-3} pc. In an attempt to estimate the density in observed structures, predictions of both shock models and photodissociation region models have been compared with measured emission brightness in the H_2 $v = 1{-}0$ $S(1)$ line. Magnetic (C-type) shocks with velocities of 30 km s^{-1} and pre-shock densities of 10^6 cm^{-3} yield the best representation of our data, notwithstanding significant discrepancies for the brightness ratio between $v = 2{-}1$ $S(1)$ and $v = 1{-}0$ $S(1)$ lines. Our results show that post-shock densities are several times 10^7 cm^{-3}. This is sufficiently high that the passage of C-type shocks in Orion yields gravitational instability which may in turn trigger star formation in the post-shock gas.

Key words. ISM: individual objects: OMC1 – ISM: kinematics and dynamics – ISM: molecules – shock waves – infrared: ISM: lines and bands

1. Introduction

The Orion Molecular Cloud (OMC1), located at a distance of 430 pc (Warren & Hesser 1977), is a region in which massive stars are forming within dense clouds of dusty molecular material. Whilst all stars undergo early in their history a period of violent ejection of material, massive stars have an especially dramatic influence on nearby molecular clouds, through shocks caused by fast outflows and the intense ultraviolet radiation field associated with high stellar surface temperatures. The outcome of these interactions is important in understanding the cycle of star formation in which massive stars form and, by perturbing their surroundings, influence the nature of the gas in which future stars may form. In particular by compressing material in nearby clouds, massive stars may serve to trigger the formation of a population of solar mass stars. The influence of fast outflows on the neighbouring material relates to two central questions in star formation. These are the factors which determine the initial mass function (IMF) for star formation (e.g. Elmegreen 1999) and the related problem of the fraction of stars which form in clusters, rather than individually (e.g. Brandl et al. 1999). In Orion and elsewhere (e.g. NGC 3603; Brandl et al. 1999) there tend to be a small number of OB associations and a very large number of normal stars in the vicinity. For example in the Trapezium cluster in Orion, there are more than 700 stars (see O'Dell et al. 1997 and references therein). One goal of our work is to examine in detail the structures that form in perturbed gas around massive young stars in OMC1. In addition we investigate the proposition that the perturbations caused by massive stars may generate an environment involving gravitational instability which may trigger star formation in the surrounding material.

The region for which observations are reported here covers an area to the north of the Trapezium stars in a highly obscured dusty zone to the south east of IRc2 and the Becklin-Neugebauer Object (BN). This region and

Send offprint requests to: D. Field, e-mail: dfield@ifa.au.dk
⋆ Visiting astronomers (JLL and DF) at the European Southern Observatory, La Silla, Chile.

similar regions to the north-west have been very extensively studied in recent years, and are known to contain complex structure. In common with a number of these studies, we report observations of rovibrational emission of molecular hydrogen. Vibrationally excited H_2 emission is a valuable tool since it probes strongly perturbed gas and involves the major molecular component of the material, providing data at sub-arcsecond resolution. Overviews of the region, showing the relative positions of BN, IRc2 and other features may be found in Schild et al. (1997); Stolovy et al. (1998) and Schultz et al. (1999).

Our review of previous work concerning this region is limited to recent comparable studies, largely involving H_2 emission but drawing on other material as appropriate. It is possible to identify three types of object within a typical field which shows H_2 emission. These are the Orion "bullets" with their associated wakes ("fingers"), so-called photo-evaporating circumstellar disks (sometimes called protoplanetary disks or "proplyds") and shocked gas in the ambient molecular cloud. The Orion bullets and fingers were first recorded in the spectacular observations of Allen & Burton (1993). These features, which are essentially Herbig-Haro (HH) objects, have been very thoroughly studied with respect to velocity profiles, morphology and most recently proper motions (e.g. Lee & Burton 1999; Tedds et al. 1999; Chrysostomou et al. 1997). Bullets have also been observed in CO (2–1) emission and are correlated spatially with H_2O maser emission in this region (Rodriguez-Franco et al. 1999; Gaume et al. 1998; Genzel & Downes 1977). The favored description of the bullets is that they arise in situ in the outflowing material through hydrodynamic instabilities (Stone et al. 1995), with densities of 2 to 3 10^5 cm^{-3} and masses of a few times 10^{-3} solar masses (Chrysostomou et al. 1997), moving with speeds relative to the background gas of $\sim$200 km s^{-1} (Lee & Burton 1999).

Photo-evaporating circumstellar disks, which are young stars with circumstellar material, have also been very intensively studied since their original identification (O'Dell et al. 1993; O'Dell & Wen 1994; McCaughrean & O'Dell 1996; McCaughrean et al. 1998; Bally et al. 1998; Henney & O'Dell 1999; Simon et al. 1999). The incentive is that the study of these objects provides a route to the understanding of planetary formation in the stellar nebula around a young stellar object. Objects have been observed in H_2 $v = 1{-}0$ $S(1)$ emission at 2.121 μm (e.g. Chen et al. 1998). The most heavily studied are those which have been exposed to view through the action of the Trapezium stars, notably the brightest, θ^1C Ori. Detailed models have been made of these (Henney & O'Dell 1999; Störzer & Hollenbach 1999). A significant number of these objects however also reside in more shielded regions (Bally et al. 1998) and one is recorded in our field (Stolovy et al. 1998: see Sect. 4.2).

The final member of this menagerie, and one that seems recently to have been somewhat neglected by observers perhaps through familiarity, is the material of the ambient molecular cloud itself. This is the material left over from that from which the perturbing OB stars must have formed. The presence of dense molecular material in the region in which the present observations were made is demonstrated by the VLA data for NH_3 of Wiseman & Ho (1996, 1998). These observations show that material is in the form of dense warm clumps on the ten arcsecond scale, where 1″ is $\sim$2.1 10^{-3} pc at the distance of OMC1. Some clumped regions exhibit large velocity gradients. These gradients show that the very active nature of the OMC1 region, apparent from H_2 emission data, is repeated on the larger scales probed by the radio observations.

OMC1 is the archetype of shocked regions yielding H_2 vibrational emission (Gautier et al. 1976). A great deal of theoretical work has been performed concerning the nature of shocks in OMC1 (e.g. Smith et al. 1991), for example in conjunction with velocity-resolved imaging of H_2 emission (Chrysostomou et al. 1997). Models have tended to explore fast shocks, for example of 200 km s^{-1}, in order to explain the very broad profiles of H_2 emission lines, which have a total extent of up to 150 km s^{-1}. Earlier attempts to model lineshapes, emission line brightness (specific intensity) ratios and absolute brightness in terms of a global outflow, reviewed in some detail in Salas et al. (1999), have not proved successful. Salas et al. (1999) however suggest that the following scenario matches their spectrally (24 km s^{-1}) and spatially (2″) resolved data for the H_2 $v = 1{-}0$ $S(1)$ line in this region. A 230 km s^{-1} spherical wind emanates from IRc2/BN impinging on a clumpy molecular cloud, where clumps have a preshock density of between 5 and 6 10^5 cm^{-3}. Bullets, developing in the outflow (Stone et al. 1995), tend to pass between the clumps, where their passage is relatively unimpeded, in keeping with the observations of Wiseman & Ho (1998). Where the wind impinges on a dense clump, an induced shock propagates into the clump with a shock speed of $\sim$20 km s^{-1}, yielding the observed line emission in these regions via a J-type shock.

This brief introduction into some of the more recent results for the IRc2/BN region of OMC1 is followed by a description of our observations and techniques of data reduction. The analysis of our results proceeds first through a detailed consideration of the scale size of structure in our images. We then consider how the high brightness of our observed H_2 emission could have been generated, including photon excitation, as in photodissociation regions (PDRs), and C- and J-type shocks.

2. Observations and data reduction

A finding chart for our observations of OMC1, taken in the $v = 1{-}0$ $S(1)$ line of H_2 at 2.121 μm, is given in Fig. 1, showing the position of the area observed relative to the Trapezium stars and a reference star TCC0016. The brightest part of our observed H_2 emission is centered around 10″ E, 0″ N of TCC0016 and is the region originally designated as "Peak 2" in Beckwith et al. (1978).

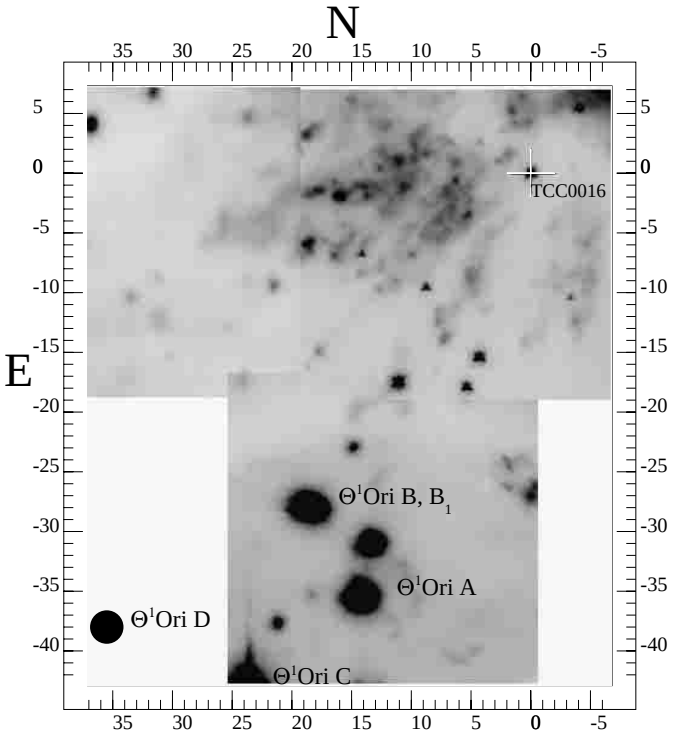

Fig. 1. A finding chart for our observations of H_2 emission, located in an area extending approximately 10″ to the West, 35″ to the East, 5″ to the North and 20″ to the south of TCC0016 (marked as a white cross). TCC0016 lies at $05^h35^m14.909^s$, $-05^0 22' 39.31''$ (J2000). The positions of the Trapezium stars are also shown relative to TCC0016

The ADONIS Adaptive Optics (AO) system at the ESO 3.6 m telescope was used for two series of observing runs on 27th to 29th December 1996 and on 12th to 14th January 1998. In both runs, ADONIS was equipped with the infrared Sharp-NICMOS camera (256×256 pixels). In Dec. 96, the seeing was exceptionally good, lying between 0.3 and 0.4 arcsec, and the lens set was used which gave a spatial resolution of 50 mas/pixel with a field of view of 12.8×12.8 arcsec. Data have been taken for nine different lines in H_2 in the K-band. In the present work we report the structure associated with the strongest line, H_2 $v = 1{-}0$ $S(1)$ at 2.121 μm, drawing upon some preliminary data for the $v = 2{-}1$ $S(1)$ line at 2.247 μm in our interpretation of the emission brightness. Results involving other lines will be reported elsewhere (work in preparation). In Jan. 98, as the seeing was relatively poor, varying between 0.8″ and 1.0″, data were recorded with the lens set giving 100 mas/pixel resolution with a field of view 25.6×25.6 arcsec. In both sets of data, spectral isolation of the 2.121 μm line and observation of the continuum at 2.179 μm were achieved using a Fabry-Perot interferometer with a resolution of $\lambda/1000$.

The extent of the field which we were able to observe was restricted by the availability of only a single star, θ^1 B Ori, as a sufficiently bright reference for wavefront sensing. The total field is of size $\sim$40″ by 25″, lying to the SE of BN/IRc2 (Fig. 1). The Strehl ratio, the ratio of the peak intensity of the measured point-spread function (PSF) to the theoretical maximum for a telescope with perfect optics and no atmosphere, diminishes as the distance from the reference star increases. θ^1 Ori B is at the south-eastern corner of our image, with the north-west corner of our field $\sim$45 arcsec away. This corresponds to a size of the order of that of the isoplanatic patch at 2 μm, the area beyond which it is generally considered that AO correction is significantly degraded. The size of the isoplanatic patch depends on the outer scale of turbulence, a poorly characterized parameter, and much larger isoplanatic patches have been reported. It is therefore not surprising that the remarkable seeing conditions, which prevailed in the Dec. 96 observations (see above), allowed us to achieve diffraction limited correction throughout the field including faint objects, so far as we were able to ascertain. The resolution in our images corresponds to a Strehl ratio between 0.37 and 0.5. In order to obtain a representative point spread function, we chose to record θ^1 Ori D to the SE (see Fig. 1), rather than θ^1 Ori B, since θ^1 Ori D lies at a distance from our field more representative for the full field than θ^1 Ori B. Numerous observations were performed of θ^1 Ori D throughout data taking, since it is important for data reduction to use a psf appropriate to the time of, and therefore the seeing for, any particular frame.

Data reduction to obtain a H_2 image was performed so as to take account of any temporal variability of the sky background, spatial variations in the sensitivity of the detector (flat-fielding), differences in the sky brightness at different wavelengths and differing efficiencies of the detection system for the different Fabry-Perot settings. Dark counts were also subtracted and bad pixels and noise due to cosmic rays removed.

Frames at the H_2 $v = 1{-}0$ $S(1)$ wavelength of 2.121 μm, and at 2.179 μm in the continuum, were deconvolved with the appropriate point-spread functions, using the technique of Subtractive Optimally Localized Averages, SOLA (Pijpers 1999). This method has been shown to preserve the smallest scales in the data more effectively than the standard methods of Maximum Entropy and Richardson-Lucy (Vannier et al. 2000; Hook 1999 and references therein). SOLA is therefore the method of choice in the present study, since we seek to investigate as large a range of scale as feasible. Implementation of SOLA involves as input some "target" resolution which it is the aim of deconvolution to achieve. If this target represents too high a resolution, the penalty will be an unacceptable level of noise. In the present data we were able, with acceptable noise, to achieve a resolution, uniform within the image, of 0.15″ for the "high resolution" data of Dec. 96 and 0.38″ for the "low resolution data" of Jan. 98. Absolute fluxes in these images were obtained by calibration using both the standard star HD 71264, at $08^h26^m18.15^s$, $-05^0 51' 49.8''$ (J2000), with a K magnitude of 8.538 (DENIS Standard Stars: see `http://denisexg.obspm.fr/standard_jk_old.html`)

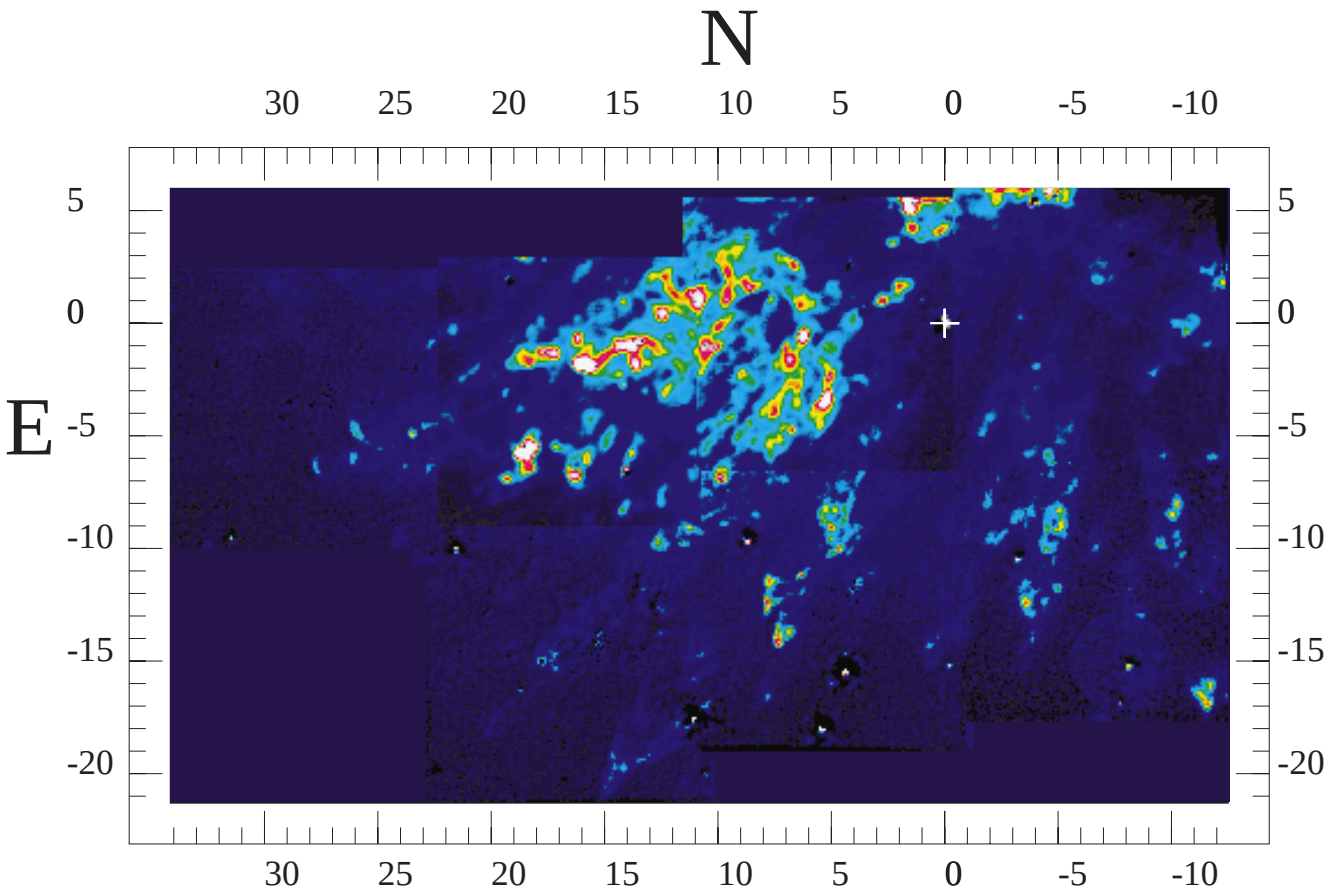

Fig. 2. The full field, comprising 7 separate 12.8″ 12.8″ fields, of H_2 emission in the $v = 1{-}0$ $S(1)$ line at 2.121 μm. Background emission has been subtracted. The data have been deconvolved and are displayed at a resolution of 0.15″ as described in the text. The white cross shows the position of TCC0016: see Fig. 1

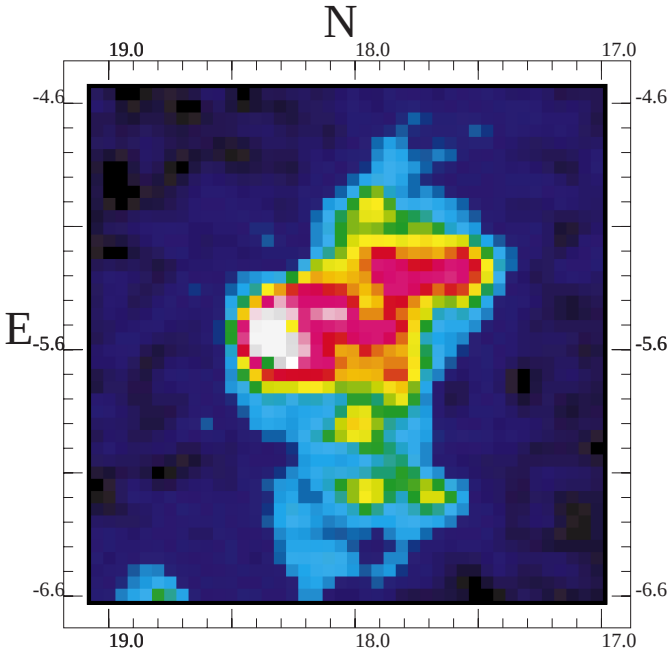

Fig. 3. A detailed view of the $v = 1{-}0$ $S(1)$ H_2 emission in Fig. 2 at a position centred on 18″ E, 5.6″ S

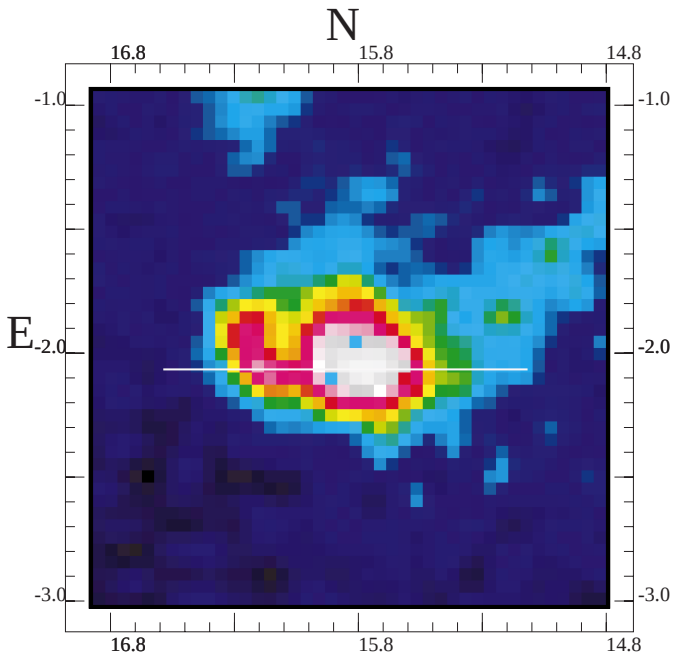

Fig. 4. A detailed view of the $v = 1{-}0$ $S(1)$ H_2 emission in Fig. 2 at a position centered on 15.8″ E, 2.0″ S. This is brightest region in our field with a peak brightness of 3.0(± 0.15) 10^{-5} $Wm^{-2}\,sr^{-1}$ (see Fig. 5). The line shows the position of the cut in Fig. 5

and TCC0016, whose K' band calibration is given in McCaughrean & Stauffer (1994). Line emission maps for the $v = 1{-}0$ $S(1)$ line were obtained for both the high and low resolution data by subtraction of the deconvolved continuum images at 2.179 μm from those at 2.121 μm. The high resolution data consisted of 7 overlapping frames. These data are shown combined in Fig. 2. A number of the strong emission features shown in Fig. 2 may be also be identified in the somewhat lower spatial resolution data presented in Schultz et al. (1999). The continuum itself shows very little emission save that from stars in the field. The region is strongly illuminated by the Trapezium stars (see Sect. 4.1) and absence of continuum emission indicates that very small dust particles, which show bright K-band emission in PDRs (e.g. NGC 7023: Lemaire et al. 1996), are absent in this part of OMC1.

Two of the brightest regions in the image in Fig. 2 are shown in more detail in Figs. 3 and 4. A cut through the image in Fig. 4 is shown in Fig. 5. This cut shows the very small scale of between 1 and 2 pixels over which large variations in surface brightness are encountered. Figure 5 also serves to calibrate the colour-coded brightness scale in Fig. 4. The brightest part of the image in Fig. 2, shown in detail in Fig. 4, has a peak surface brightness in 3×3 pixels ($0.15'' \times 0.15''$) of $3.0(\pm\ 0.15)\ 10^{-5}$ $\mathrm{Wm^{-2}\,sr^{-1}}$. The corresponding column density of the $J = 3$, $v = 1$ rovibrational level of H_2, given by $(4\pi\lambda/\mathrm{hc})I/A$, where I is the observed brightness and A the Einstein A-value for the $v = 1{-}0$ $S(1)$ line ($3.47\ 10^{-7}$ $\mathrm{s^{-1}}$; Wolniewicz et al. 1998), is therefore $1.2(\pm\ 0.06)\ 10^{18}$ $\mathrm{cm^{-2}}$. This value is a lower limit since no account has been taken of extinction in our estimate. Extinction in OMC1 can be as great as unity or more according to Rosenthal et al. (2000) (see Sect. 4.3).

We have compared our measured surface brightness to the HST observations of Stolovy et al. (1998) (S98) and we find agreement to within 10%, after corrections were made to the intensities reported in S98 (Stolovy: private communication). This comparison was made in overlapping regions between the data presented here and those in S98. For example the object reported as a photo-evaporating circumstellar disk 154–240 (O'Dell et al. 1997; O'Dell & Wen 1994) at $05^{\mathrm{h}}35^{\mathrm{m}}15.4^{\mathrm{s}}$, $-0.5^{0}22'40''$ (J2000) shown in Figs. 1 and 5b in S98 may also be found in our image, at an offset 6.1″ E, 0.6″ S.

3. Discussion of results: Sizes of structures

Our first goal is to characterize the nature of the structure in our observed image of the H_2 $v = 1{-}0$ $S(1)$ emission. Bullets (Herbig-Haro objects), photo-evaporating circumstellar disks and ambient shocked cloud material may each exhibit H_2 emission and each may have a characteristic and different size distribution. However, in our field, there is only one object which has been assigned as a photo-evaporating circumstellar disk, 154–240 mentioned above. The Orion bullets are found in two groups to the north of BN/IRc2 and to the south of the Trapezium stars (O'Dell et al. 1997). There are no known bullets in our field. Therefore we assume that the emission in our image arises to a very large degree from a single type of object, that is, from shocked and irradiated ambient material.

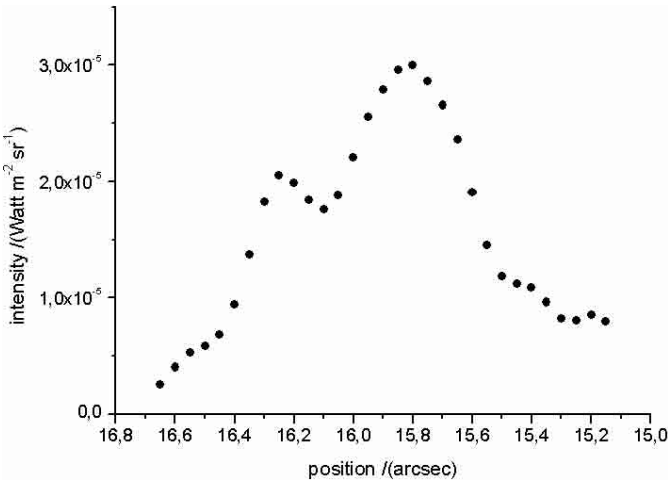

Fig. 5. A cut through the image in Fig. 4, showing the variation of brightness with position in the region of maximum brightness in the image in Fig. 2

There have been numerous studies in recent years of structure in molecular clouds. A number of powerful tools have been developed to establish if clouds show a fractal distribution, or otherwise, of the scale sizes and masses of internal structures (see for example Williams et al. 1999; Elmegreen & Falgarone 1996). In particular it has been found that a fractal image, displaying so-called "fractional Brownian motion", may be defined as one whose Fourier transform displays random phases. In addition fractal images have been shown to have power spectra, $P(k)$, in the inverse scale length, wave vector k, which follow a power law $P(k) \propto \mid k \mid^{-\beta}$ (Stutzki et al. 1998 and references therein). With respect to observations of H_2, Rouan et al. (1997) found that H_2 emission in the $v = 1{-}0$ $S(1)$ line, close to the exciting star in the photodissociation region in NGC 2023, showed such a power law dependence in the wave vector.

In the present section, we show that the distribution of sizes of structure in Fig. 2 departs from a fractal and we establish preferred scales in this region. We use 3 independent techniques to examine structure in our image in Fig. 2. These are an area-perimeter analysis, a Fourier transform technique and a histogram technique described in Blitz & Williams (1997). As an additional check we also make direct measurements of the size of structures in Fig. 2.

3.1. Area-perimeter analysis

Area-perimeter analysis was performed as follows. For each feature of sufficient brightness in Fig. 2, we seek to find a set of perimeters with each set corresponding to perimeters delineated by different levels of brightness. Various levels of brightness were chosen, corresponding

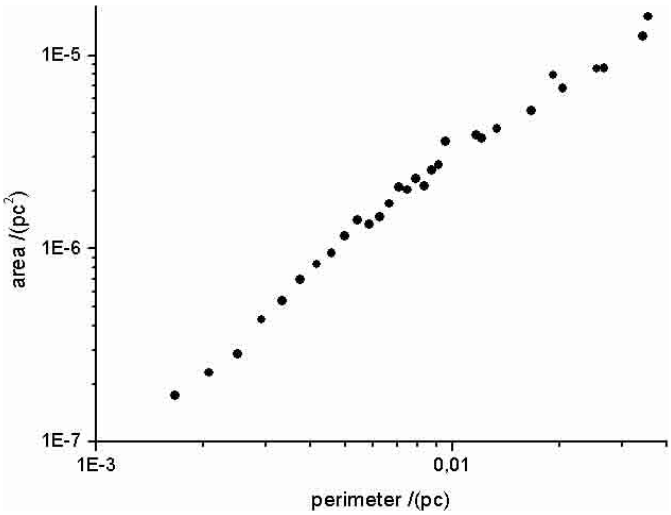

Fig. 6. Area-perimeter analysis (Sect. 3.1): the variation of the area vs. the perimeter for structures identified in the "low" resolution H_2 $v = 1{-}0$ $S(1)$ emission data of Jan. 98

to between 500 and 1000 counts per pixel in steps of 100 (where counts correspond to 100 s integration time). For reference, the brightest pixel in the field contains ∼2500 counts. To perform our analysis, a set of images was created with all counts set to zero in those pixels whose counts were below a chosen level and all others set to some common (arbitrary) value. With respect to measurement of the perimeter of any object at any chosen brightness level, we note that 1, 2 or 3 sides of a pixel on the perimeter may contribute to the perimeter. A 3×3 pixel filter has therefore been devised which, on convolution with each image, identifies the category into which each pixel on the perimeter falls and allows direct evaluation of the perimeter. This procedure enabled us to tabulate the area vs. the perimeter as a function of the set level of perimeter-defining brightness for every structure above noise in the image.

A log–log plot of area versus perimeter was constructed and is shown in Fig. 6 using data from the "low" resolution observations of Jan. 98; the higher resolution data of Dec. 96 show similar behaviour. For clarity in Fig. 6, for any particular perimeter for any set of features, we show the average area rather than individual areas. Figure 6 displays significant curvature: for example if the values for larger perimeters, e.g. $\geq$ 1.75 10^{-2} pc, and areas are linearly extrapolated to a perimeter value of (say) 2 10^{-3} pc, then the observed area falls below the extrapolated line by a factor of more than 3. Uncertainties, associated with the determination of perimeter and area, arise from noise in our data. These uncertainties are however only comparable with the size of the symbols in Fig. 6.

As a check on the procedures used to create the data in Fig. 6, fractal images were prepared using a power spectrum $P(k) \propto \mid k \mid^{-\beta}$ with random phase associated with each position in the image. Inverse Fourier-transform yielded a fractal. Area-perimeter plots showed linear log–log plots and a dimension, d, derived from perimeter $\propto$ (area)$^{d/2}$, which satisfied the required relationship $d = 3 - \beta/2$ (Stutzki et al. 1998).

3.2. Fourier analysis

A two-dimensional Fourier transform has been used to form a power spectrum, $P(k)$, of the objects in Fig. 2. In contrast to the area-perimeter analysis, Fourier amplitudes take into account the brightness encountered at the corresponding scale. Ln($P(k)$) obtained in this manner shows marked departure from a power law in k, corroborating the finding of the area-perimeter analysis. Since the slope of ln($P(k)$) vs. ln k is roughly 2, a plot of ln $k^2P(k)$ vs. ln k emphasizes the departure of the distribution from power law behaviour. Results are shown in Fig. 7 for the "low" resolution H_2 $v = 1{-}0$ $S(1)$ emission data of Jan. 98. Figure 8 shows a similar plot for the high resolution data of Dec. 96. A fractal distribution, in contrast to our data, would show a straight line dependence with a slope of $(2 - \beta)$. In order to check this, a fractal has been constructed as in Sect. 3.1 but in the same field of view as the Dec. 96 observations, that is, $12.8'' \times 12.8''$. This model has been convolved with an observed PSF and 5% Poisson noise with 5% white noise added. The resulting data have been deconvolved with SOLA, using a target PSF of $0.15''$, mimicking our data treatment. The power spectrum of this image, plotted as ln $k^2P(k)$ vs. ln k, shows a straight line with a slope of $2 - \beta$, as expected for a fractal. In addition, the noise that has been added to the image causes a peak to form below a scale of ∼5 10^{-4} pc with a maximum at 3.5 10^{-4} pc. A similar peak due to noise is apparent in our data and its inception is visible for example in Fig. 8. For this reason data are not displayed at smaller scales. A similar phenomenon occurs in Fig. 7, at slightly smaller scales, since these data are of higher signal-to-noise.

Figures 7 and 8 show that there is a range of scales excessively populated, compared with a fractal. This range has a broad maximum around a central value of ∼3 10^{-3} pc, that is, $\sim 1.4''$. Since Figs. 7 and 8 both yield essentially the same result, artefacts due for example to edge effects do not contribute significantly in our analysis.

3.3. A brightness histogram technique

The third method of investigation is based on that first described in Blitz & Williams (1997: BW97). This technique involves counting the number of pixels, binned into some small brightness range, as a function of pixel brightness. Essentially BW97 points out that a plot of the number of pixels, $N(B_n)$ vs. B_n, the normalized brightness, should yield a curve which remains unchanged for an image with no preferred scale, when the resolution of the image is degraded. The normalized brightness is defined as the value of brightness divided by the value in the brightest pixel

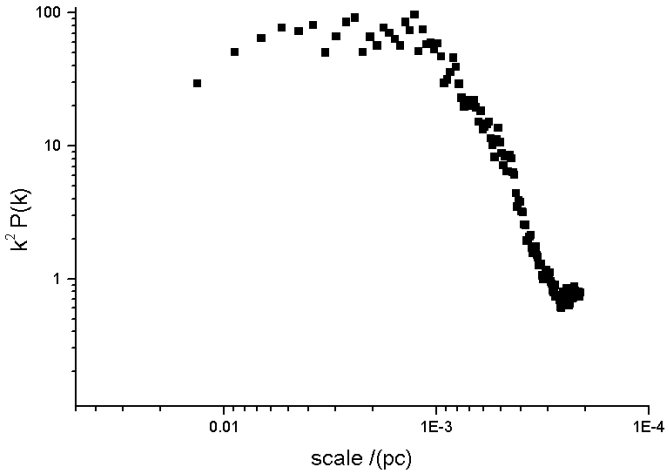

Fig. 7. Fourier analysis (Sect. 3.2): the power spectrum, multiplied by k^2, vs. the scale size of structures, obtained using the "low" resolution H_2 $v = 1{-}0$ $S(1)$ emission data of Jan. 98

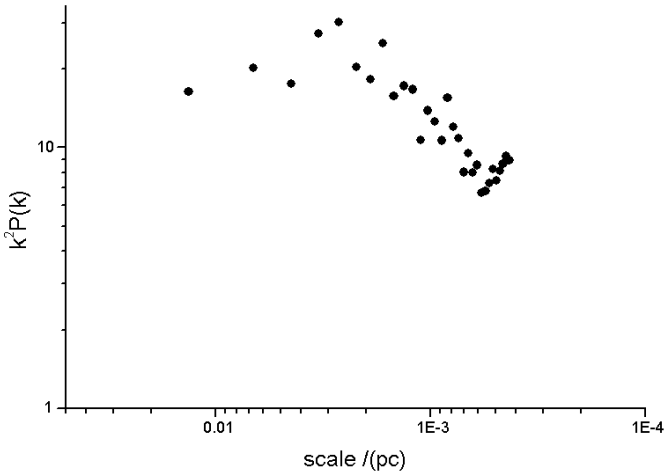

Fig. 8. Fourier analysis (Sect. 3.2): the power spectrum, multiplied by k^2, vs. the scale size of structures, obtained using the high resolution H_2 $v = 1{-}0$ $S(1)$ emission data in Fig. 2

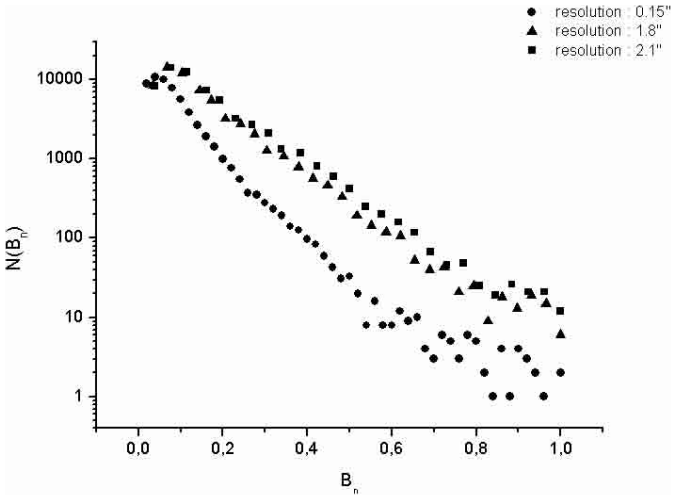

Fig. 9. Brightness histogram technique (Sect. 3.3): the number of pixels, $N(B_n)$, vs. B_n, the normalized brightness, for the high resolution H_2 $v = 1{-}0$ $S(1)$ data of Fig. 2 for a spatial resolution of $0.15''$ and with resolution degraded as shown

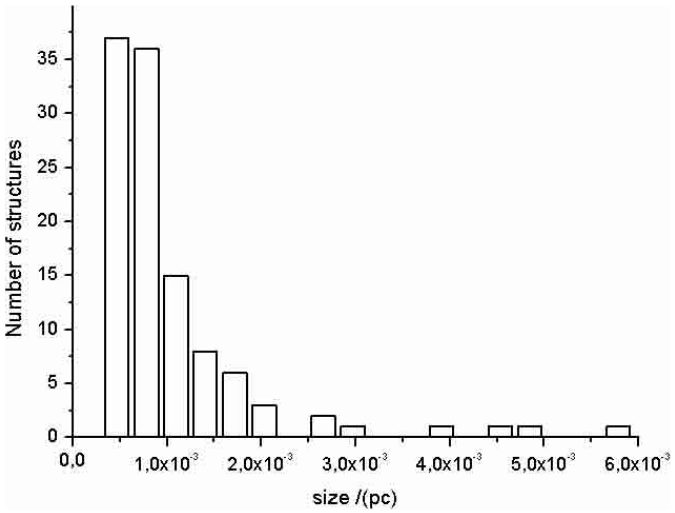

Fig. 10. Direct measurement of structures (Sect. 3.4): a histogram of sizes of structures, obtained using the high resolution H_2 $v = 1{-}0$ $S(1)$ emission data in Fig. 2

in the image. In contrast, for an image with a preferred scale, such a plot should change its form as resolution is degraded to the point at which any preferred scale has been artificially washed out. Beyond this critical smoothing, the form of $N(B_n)$ vs. B_n should be independent of the degree of smoothing. The amplitude of the critical smoothing is a direct measure of the preferred scale size of structure in the image.

The lower curve in Fig. 9 represents log $n(B_n)$ vs. B_n for the data in Fig. 2, where a log plot has been used to show the full range of data. The upper curve shows data degraded in resolution by a factor of 14, which we have found to be the critical degree of smoothing. For comparison the intermediate curve shows data degraded in resolution by a factor of 12. Thus the method of BW97 suggests that we have objects in our image at a preferred scale of $\sim 4.25 \pm 0.2\ 10^{-3}$ pc, that is $\sim 2''$. This is a similar scale to that identified by the Fourier transform method, serving as a useful check on the validity of our interpretation of the Fourier results.

We have examined the behaviour of the above technique with the synthetic fractal image used to test the Fourier analysis technique in Sect. 3.2. This image by definition must have no preferred scale. Using the image, the form of $N(B_n)$ vs. B_n was indeed found to be independent of introduction of numerical smoothing. This is a useful validation of the BW97 method as a means of determining the preferred scale in an image. Further discussion of this technique may be found in Williams (1998), Blitz & Williams (1999) and Williams et al. (1999), who have also tested fractal and non-fractal images.

3.4. Direct measurements of structures

Direct measurement of the number of structures of a certain size in Fig. 2 was performed by locating features whose maximum brightness was greater than 4 times the background brightness in the image. The background was obtained from a suitable dark area of the image in Fig. 2. In order to estimate the size of any object thus located, the area, A, was estimated which was enclosed by the perimeter defined by half the maximum intensity. The linear dimension of a feature was accorded a value of $(A)^{1/2}$. In contrast to the Fourier analysis, this yields a distribution of sizes which is independent of the brightness of the features involved. A histogram of sizes obtained by binning features into groups differing by 3 pixels ($0.15''$; $3\ 10^{-4}$ pc) in linear dimension is shown in Fig. 10. The data in Fig. 10 show that there are only a small number (9) of these larger structures of scale $> 2\ 10^{-3}$ pc that can be identified on the basis of the direct counting method.

The conclusions which we draw from the above analyses are (i) that structure is not fractal, differing in this respect from a number of high resolution images previously reported (Stutzki et al. 1998 and references therein) and (ii) that there is a population of objects of characteristic scale $3\ 10^{-3}$ to $4\ 10^{-3}$ pc. The non-fractal nature of the medium is consistent with the material being gravitationally bound, an issue which is discussed in more detail below with reference to both scale sizes and densities.

4. Discussion of results: Emission brightness

This section describes our attempts to use absolute brightness of H_2 emission to estimate the mean density where clumps of material are found. Our aim is to establishing whether gravitational instability may ensue, as a first step to star formation. In this connection a census of stars (McCaughrean & Stauffer 1994), in a 0.2×0.2 pc region centered on the Trapezium OB stars, yields a stellar density of $4.7\ 10^4$ stars per cubic parsec. Thus one would broadly expect to encounter a single star in a volume of $12.8'' \times 12.8'' \times 12.8''$, that is, in a volume that may crudely be associated with one of our frames. Hence the suggestion that within our image there may be one or two structures which may at some future date form stars is consistent with the known stellar density in this general region. One star may indeed have formed, that is, in the photo-evaporating circumstellar disk 154–240, if this may be correctly identified as a young star (see Sect. 4.2).

The average peak brightness of the fourteen brightest objects in Fig. 2 is $1.25\ 10^{-5}$ $\mathrm{Wm^{-2}\,sr^{-1}}$. In addition, data taken in the $v = 2{-}1$ $S(1)$ transition at 2.247 μm show mean values of brightness 7 ± 2 times weaker than in the $v = 1{-}0$ line, in regions of bright $v = 1{-}0$ $S(1)$ emission. Models are required which can reproduce both the observed values of brightness, up to the maximum of $3\ 10^{-5}\,\mathrm{Wm^{-2}\,sr^{-1}}$ (Fig. 5), and also the $v = 1{-}0/v = 2{-}1$ line ratio. The influence of extinction in the K-band is briefly considered in Sect. 4.3.

The bright H_2 emission observed may be caused by the proximity of O- and B-stars, which yield H_2 emission through a fluorescence mechanism (Black & Dalgarno 1976; Hollenbach & Tielens 1999 and references therein) and through heating (Störzer & Hollenbach 1999, hereafter SH99). Alternatively the bright H_2 emission may be excited through the action of shocks caused by material playing upon the ambient molecular cloud, as discussed in the introduction.

4.1. Photodissociation region models

The measured H_2 surface brightness of $1.25\ 10^{-5}$ $\mathrm{Wm^{-2}\,sr^{-1}}$ in the $v = 1{-}0$ $S(1)$ line surpasses that associated with bright photodissociation regions (PDRs) in which the fluorescence mechanism dominates, such as peaks in the PDR in NGC 7023 (Lemaire et al. 1996), by more than an order of magnitude. Turning to observations of a photo-evaporating circumstellar disk (182–413) illuminated and heated by the O-star θ^1C Ori in the Trapezium cluster (Chen et al. 1998), values of brightness recorded at 2.121 μm lie between 2 to $3\ 10^{-6}$ $\mathrm{Wm^{-2}\,sr^{-1}}$, that is ∼20% of the value of average brightness of our bright objects and ∼8% of the brightest object.

Models of the photo-evaporating circumstellar disk 182–413 and other similar PDRs discussed in SH99 give useful information for our present work, albeit these calculations are strictly relevant only to the environment of those disks. SH99 reproduce the brightness observed by Chen et al. (1998) for gas of number density $(n(\mathrm{H})+2n(\mathrm{H_2}))$ $4\ 10^6$ $\mathrm{cm^{-3}}$ and a radiation field with an intensity corresponding to $2.4\ 10^5$ times the standard interstellar field ($G_0 = 2.4\ 10^5$). In our case, our region is exposed to the field of the Trapezium stars, which lie at a distance of around 0.1 pc. This corresponds to $G_0 \sim 2\ 10^5$ including appropriate attenuation by dust in the HII outflow as discussed in SH99. Since the conditions are much as for 182–413, results in SH99 therefore show that illumination by the Trapezium stars yields only a small proportion of our observed emission at 2.121 μm, noting that calculated brightness is insensitive to increase in G_0 or number density above the figures mentioned. SH99 record that emission in the $v = 2{-}1$ $S(1)$ line would be ∼7 times weaker than in the $v = 1{-}0$ $S(1)$ line, a ratio which agrees with our observations.

Results in SH99 also show that if there were an O-star comparable to θ^1C Ori at a distance of 0.01 pc (5 arcsec) from a clump of gas, irradiated without shielding, and an ambient density of $2\ 10^7$ $\mathrm{cm^{-3}}$ with several $\mathrm{km\,s^{-1}}$ of advection within the H_2 emitting zone (Lemaire et al. 1999), this would yield ∼60% of the average peak brightness of $1.25\ 10^{-5}$ $\mathrm{Wm^{-2}\,sr^{-1}}$ in our region. While this remains less than 25% of the brightness of our brightest region, the presence of close-by obscured massive stars with the associated heating effects of advection may turn out to play a role in a fuller understanding of our observations.

However obscuration of an O-star would imply very large local column densities of material. We discuss this further below in connection with the photo-evaporating circumstellar disk 154–240.

4.2. The photo-evaporating circumstellar disk 154–240

Some support for the presence of a nearby O-star comes from a consideration of the emission of the globule of gas at position 6″ E, 0.6″ S, designated the photo-evaporating circumstellar disk 154–240 in O'Dell et al. (1997). We find that the peak brightness of emission in this object is 1.2 10^{-5} $\mathrm{Wm^{-2}\,sr^{-1}}$ in the $v = 1{-}0$ $S(1)$ line and 7 10^{-7} $\mathrm{Wm^{-2}\,sr^{-1}}$ in the $v = 2{-}1$ $S(1)$ line. The model in SH99 mentioned above, corresponding to an O-star at a distance of 0.01 pc, an ambient density of 2 $10^7\mathrm{cm^{-3}}$ and 4.1 km $\mathrm{s^{-1}}$ of advection, yields a brightness of 7.5 10^{-6} $\mathrm{Wm^{-2}\,sr^{-1}}$ in the $v = 1{-}0$ $S(1)$ line and 4.4 10^{-7} $\mathrm{Wm^{-2}\,sr^{-1}}$ in the $v = 2{-}1$ $S(1)$ line. Thus the $v = 1{-}0/v = 2{-}1$ ratio is accurately predicted whilst the absolute brightness is too low by a factor of 1.6. According to SH99, higher advection velocities, increased G_0 or higher density would not increase the line brightness significantly. The discrepancy between observations and calculations may be removed altogether if we include background H_2 emission present in our image. This may contribute $\sim$4 10^{-6} $\mathrm{Wm^{-2}\,sr^{-1}}$ for the $v = 1{-}0$ $S(1)$ line and $\sim$2 10^{-7} $\mathrm{Wm^{-2}\,sr^{-1}}$ for the $v = 2-1$ $S(1)$ line in the line-of-sight. The calculated values for the model in SH99 then agree within observational error with the observed line brightness for both $v = 1{-}0$ and $v = 2{-}1$ $S(1)$ lines in 154–240.

Is there any evidence for an exciting source close to 154–240? Our continuum image shows the presence of an object, which we assume to be a star rather than a globule of hot dust (say), with a brightness of $\sim$2.4 10^{-5} $\mathrm{Wm^{-2}\,sr^{-1}}$, lying at a projected distance in plane of the sky of 9 10^{-3} pc from 154–240. This object is sufficiently obscured in the visible to be absent from the HST survey of stars in this region (Prosser et al. 1994) which was sensitive to a visual magnitude of $\sim$20. If we assume that this object is an O-star with $T_{\mathrm{eff}} = 50\,000$ K, our observations would require an opacity at 2 μm of $\sim$21.6. This corresponds to a number density of 3.5 10^7 $\mathrm{cm^{-3}}$ over a distance of 0.01 pc and a local column density of $\sim 10^{24}$ $\mathrm{cm^{-2}}$. Whilst a local inhomogeneity of this nature cannot be excluded, this value is 2 orders of magnitude greater than the average figure that has been suggested (Rosenthal et al. 2000) for the similar area to the north of OMC1. In addition a somewhat contrived geometry must be invoked in order that an O-star be both obscured to view but able to illuminate 154–240. Our reservations with regard to both obscuration and geometry apply equally to the excitation of 154–240 and to the general role of PDR contributions to H_2 emission in the entire field.

4.3. The rôle of shocks

A grid of calculations has been performed for both J-type and C-type shocks, in planar geometry. In these models the dynamical equations and chemical rate equations are solved in parallel, thus allowing for the variation in fractional ionization in the gas within the shock wave, a factor of importance for C-type shocks. Cooling rates are treated in a detailed manner taking account of all important chemical species. More information may be found in Flower & Pineau des Forêts (1999). Full results may be obtained electronically via information supplied in Wilgenbus et al. (2000) or via the Collaborative Computational Project No 7 (CCP7) at `http://ccp7.dur.ac.uk/pubs.html`.

For J-type shocks, the maximum brightness which we obtain is for a shock of 20 $\mathrm{km\,s^{-1}}$ impacting on material of pre-shock density 5 10^6 $\mathrm{cm^{-3}}$, a model reminiscent of that of Salas et al. (1999) but with a higher preshock density. Our shock model yields a post-shock density of 7.6 10^8 $\mathrm{cm^{-3}}$ at 50 K and 3.8 10^9 $\mathrm{cm^{-3}}$ at 10 K. The $v = 1{-}0$ $S(1)$ line brightness, integrated along the direction of propagation of the shock, is 1.6 10^{-6} $\mathrm{Wm^{-2}\,sr^{-1}}$. The $v = 2-1$ $S(1)$ line has a brightness $\sim$3.5 times lower, making it a factor 2 brighter relative to the $v = 1{-}0$ line than our observations show. The $v = 1{-}0$ $S(1)$ brightness is however a factor of $\sim$8 below the average brightness of bright objects and $\sim$20 times dimmer than the brightest object in our field. Whilst these discrepancies may be reduced to some extent if shocks are judged to be viewed edge-on rather than full-face, it would not appear possible to reconcile our observations with pure J-type shocks.

For C-type shocks, the observed H_2 brightness may be readily achieved. For example for a shock velocity of 25 $\mathrm{km\,s^{-1}}$, a pre-shock density 10^6 $\mathrm{cm^{-3}}$ gives an emission brightness of 3.3 10^{-5} $\mathrm{Wm^{-2}\,sr^{-1}}$ in $v = 1{-}0$ $S(1)$, exceeding the peak emission in the brightest region (see Fig. 5). The corresponding post-shock density is $\sim$3 10^7 $\mathrm{cm^{-3}}$ at 10 K (Wilgenbus et al. 2000). However, the $v = 2{-}1$ $S(1)$ line is calculated to have a brightness $\sim$33 times lower than that of the $v = 1{-}0$ $S(1)$ line, compared with the observed value of 7±2. If we include an extinction of unity in the IR (Rosenthal et al. 2000), then we may seek to match regions effectively $\sim$2.5 times brighter. In the case of the brightest region, this corresponds to a brightness of $\sim$7.5 10^{-5} $\mathrm{Wm^{-2}\,sr^{-1}}$. In fact, a slightly higher shock velocity of 30 $\mathrm{km\,s^{-1}}$, again with a pre-shock density 10^6 $\mathrm{cm^{-3}}$, gives an emission brightness of 7.4 10^{-5} $\mathrm{Wm^{-2}\,sr^{-1}}$. The corresponding post-shock density is $\sim$4 10^7 $\mathrm{cm^{-3}}$ at 10 K. Since the shock is now warmer, the $v = 2{-}1$ $S(1)$ line is relatively brighter, and is $\sim$16 times weaker than the $v = 1{-}0$ $S(1)$ line. This is only a factor of two too weak compared with observations. This model is presently the best available to reproduce our data.

One may question if the initial magnetic induction used in our C-type shock models is appropriate for this region of OMC1. The initial value of the transverse

magnetic induction was given by the scaling relation $B(\mu\mathrm{G}) = [n_\mathrm{H}\ (\mathrm{cm}^{-3})]^{0.5}$ (Troland & Heiles 1986). Thus in the above C-type shock computations a transverse magnetic induction of 1 mG was used. There are two measurements of the magnetic field in Orion reasonably close to the region of interest. Crutcher et al. (1999) have used CN hyperfine splitting to measure a field of magnitude 0.19 ± 0.09 mG and another undetectably weak, in a 23 arcsec beam, measurements referring to two different areas centered about 35 to 40 arcsec from the centre of our region. Norris (1984) gave an estimate of a magnetic field of 3 mG, based on the apparent velocity difference of a presumed Zeeman pair of OH masers at 1665 MHz. These masers are located at a position 24 arcsec to the NW of "peak 2", see Fig. 1. The masers in question lie midway between the regions studied by Crutcher et al. (1999). We draw the conclusion that the magnetic field is rather non-uniform in this zone and that our assumption of a field of 1 mG is acceptable. In this connection the assumption of a lower field will yield higher shock temperatures with a larger proportion of the emission in $v = 2{-}1$ compared to $v = 1{-}0$ lines, higher post-shock number density, and lower line brightness. Thus a somewhat smaller magnetic field may match our observations somewhat better. Further models will be explored in future work in an attempt to match a greater range of H_2 emission lines (work in progress).

5. Concluding comments: Gravitational instability in OMC1

The aim of the preceding section was to determine the number densities of clumps in the region observed. J-type shocks, being hotter than C-type, roughly reproduce the line ratio in $v = 2{-}1/v = 1{-}0$ emission, but fail to reproduce the brightness. The cooler C-type shocks readily reproduce the high brightness of H_2 $v = 1{-}0$, but underestimate emission in $v = 2{-}1$ $S(1)$. If we include unit extinction in IR, this underestimate may only be a factor of two. Exploration of further C-type shock models may therefore be fruitful. In addition, non-stationary state shocks may form which exhibit both C- and J-type characteristics (Pineau des Forêts & Flower 2000), a scenario which might yield both high brightness in the $v = 1{-}0$ $S(1)$ line and sufficiently warm gas for high brightness in the $v = 2{-}1$ $S(1)$ line. Turning to dense PDRs, these give too weak emission, though they are brighter than face-on J-type shocks. Dense PDRs also suffer from difficulties associated with observational constraints for obscuration of the exciting stars and special geometrical requirements. C-type shock models presently provide the best available measure of the mean density in clumps of post-shocked gas around Peak 2, which we therefore estimate to be a few times 10^7 cm^{-3}.

There is independent evidence that there is dense gas in the vicinity. There are numerous H_2O masers within 15 to 25 arcsec of Peak 2, lying between our region and BN (Genzel & Downes 1977; Gaume et al. 1998). The observations of Gaume et al. (1998), at a spatial resolution similar to ours, cover only a small portion of peak 2 and a region to the west and north, extending roughly $25'' \times 25''$. In the region in which observations overlie peak 2, there are several H_2O maser features of high flux, around position (8, 2) in Fig. 2. Masers are displaced from the radial velocities of NH_3 emission (Wiseman & Ho 1998) by $\sim$5 km s^{-1}. This velocity shift is perhaps associated with their origin in warm gas which has undergone a fast C-type shock (Elitzur et al. 1989). On the assumption that the masers probe gas belonging to the same cloud of material which yields the NH_3 emission, and by implication the H_2 emission, the presence of H_2O masers provides useful evidence of local gas of density in excess of 10^8 cm^{-3} (Yates et al. 1997).

The extensive analysis described in Sect. 3 shows that the spectrum of scales is not fractal, with preferred scales for objects of size $3\ 10^{-3}$ to $4\ 10^{-3}$ pc. The Jeans length may be expressed as $l_\mathrm{J} \sim 3.7(T/n)^{1/2}$ pc where T is the kinetic temperature and n is the number density, $n(\mathrm{H})+2n(\mathrm{H_2})$ cm^{-3} (BW97). Thus gravitational instability may arise, ignoring effects of magnetic field or of turbulent motions, if the mean number density exceeds $\sim 7.5\ 10^5$ K cm^{-3}. Post-shock gas cools rapidly within a period of a few to a few tens of years to a temperature of 10 K and gravitational instability may therefore set in for number densities in excess of $\sim 10^7$ cm^{-3}. Since post-shock densities may be several times this figure, clumps of matter, compressed through the passage of shocks, may begin to collapse under the action of gravity. The largest of the individual clumps identified contains 0.1 $M_\odot$ to 0.15 $M_\odot$ according to our present density estimates and is a candidate site for low mass star formation. Some smaller clumps may be proto-brown dwarf candidates (e.g. Simon et al. 1999; Reid et al. 1999). In summary, for the Peak 2 region in OMC1 the present work provides good evidence for the formation of dense structures and possible low mass star formation, where this is triggered by the passage of shock waves associated with fast outflows from nearby massive young stars.

Acknowledgements. We would like to thank Dr. S. Stolovy for supplying us with flux calibrated maps of H_2 emission in OMC1 for comparison with our data. We would like to thank the Director and Staff of ESO for making possible the observations reported in this paper. We would also like to acknowledge the assistance of the Particle Physics and Astronomy Research Council (UK) and the CNRS for financial assistance for one of us (DF). FPP is supported by the Theoretical Astrophysics Center, which is funded by Danmarks Grundforskningsfond and is a collaboration between Aarhus and Copenhagen Universities.

References

Allen, D. A., & Burton, M. G. 1993, Nature, 363, 54
Bally, R., Sutherland, R. S., Devine, D., & Johnstone, D. 1998, ApJ, 116, 293

Beckwith, S., Persson, S. E., Neugebauer, G., & Becklin, E. E. 1978, ApJ, 223, 464
Black, J. H., & Dalgarno, A. 1976 ApJ, 203, 132
Blitz, L., & Williams, J. P. 1997, ApJ, 488, L145
Blitz, L., & Williams, J. P. 1999, in The Origin of Stars and Planetary Systems, ed. C. J. Lada, & N. D. Kylafis, NATO Sci. Ser., Series C: vol. 540 (Kluwer Academic Publishers; Dordrecht, Boston and London)
Brandl, B., Brandner, W., Eisenhauer, F., et al. 1999, A&A, 352, L69
Chen, H., Bally, J., O'Dell, C. R., et al. 1998, ApJ, 492, L173
Chrysostomou, A., Burton, M. G., Axon, D. J., et al. 1997, MNRAS, 289, 605
Crutcher, R. M., Troland, T. H., Lazareff, B., Paubert, G., & Kazes, I. 1999, ApJ, 514, L121
Elitzur, M., Hollenbach, D. J., & McKee, C. F. 1989, ApJ, 346, 983
Elmegreen, B. G. 1999, ApJ, 515, 323
Elmegreen, B. G., & Falgarone, E. 1996, ApJ, 471, 816
Flower, D. R., & Pineau des Forêts, G. 1999, MNRAS, 308, 271; also available on the Collaborative Computational Project No. 7 (CCP7) site at `http://ccp7.dur.ac.uk/pubs.html`
Gaume, R. A., Wilson, T. L., Vrba, F. J., Johnston, K. J., & Schmid-Burgk, J. 1998, ApJ, 493, 940
Gautier, T. N., Fink, U., Treffers, R. R., & Larson, H. P. 1976, ApJ, 207, L129
Genzel, R., & Downes, D. 1977 A&A, 61, 117
Henney, W. J., & O'Dell, C. R. 1999, AJ, 118, 235
Hollenbach, D. R., & Tielens, A. G. G. M. 1999, Rev. Mod. Phys., 71, 173
Hook, R. N. 1999, ST-ECF Newsletter, 26, 3
Lee, J.-K., & Burton, M. G. 2000, MNRAS, 315, 11
Lemaire, J.-L., Field, D., Gerin, M., et al. 1996, A&A, 308, 895
Lemaire J.-L., Field D., Maillard J. P., et al. 1999, A&A, 349, 253
McCaughrean, M. J., & O'Dell, C. R. 1996, AJ, 111, 1977
McCaughrean, M. J., Chen, H., Bally, J., et al. 1998, ApJ, 492, L157
McCaughrean, M. J., & Stauffer, J. R. 1994, ApJ, 108, 1382
Norris, R. P. 1984, MNRAS, 207, 127
O'Dell, C. R., Wen, Z., & Hu, X. 1993, ApJ, 410, 696
O'Dell, C. R., & Wen, Z. 1994, ApJ, 436, 194
O'Dell, C. R., Hartigan, P., Lane, W. M., et al. 1997, AJ, 114, 730
Pijpers, F. P. 1999, MNRAS, 307, 659
Pineau des Forêts, G., & Flower, D. R. 2000, to appear in Molecular Hydrogen in Space, ed. F. Combes, & G. Pineau des Forêts
Prosser, C. F., Stauffer, J. R., Hartmann, L., et al. 1994, ApJ, 421, 517
Rodriguez-Franco, A., Martin-Pintado, J., & Wilson, T. L. 1999, A&A, 344, L57
Rosenthal, D., Bertoldi, F., & Drapatz, S. 2000, A&A, to appear
Rouan, D., Field, D., Lemaire, J.-L., et al. 1997, A&A, 284, 395
Salas, L., Rosado, M., Cruz-Gonzáles, I, et al. 1999, ApJ, 511, 822
Schild, H., Miller, S., & Tennyson, J. 1997 A&A, 318, 608
Schultz, A. S. B., Colgan, S. W. J., Erickson, E., et al. 1999, ApJ, 511, 282
Simon, M., Close, L. M., & Beck, T. L. 1999, AJ, 117, 1375
Reid, I. N., Kirkpatrick, J. D., Liebert, J., et al. 1999, ApJ, 521, 613
Smith, M. D., Brand, P. W. J. L., & Moorhouse, A., 1991, MNRAS, 248, 730
Stolovy, S. R., Burton, M. G., Erickson, E., Kaufman, M. J., et al. 1998, ApJ, 492, L151
Stone, J. M., Jianjun Xu, & Mundy, L. G. 1995, Nature, 377, 315
Störzer, H., & Hollenbach, D. J. 1999, ApJ, 515, 669
Stutzki, J., Bensch, F., Heithausen, A., Ossenkopf, V., & Zielinsky, M. 1998, A&A, 336, 697
Tedds, J. A., Brand, P. W. J . L., & Burton, M. G. 1999, MNRAS, 307, 337
Troland, T. H., & Heiles, C. 1986, ApJ, 301, 339
Wilgenbus, D., Cabrit, S., Pineau des Forêts, G., & Flower, D. R. 2000, A&A, 356, 1010
Warren, W. H., & Hesser, J. E. 1977, ApJS, 34, 115
Williams, J. P. 1998, in Interstellar Turbulence, Proceedings of the 2nd Guillermo Haro Conference, ed. J. Franco, & A. Carraminana (Cambridge University Press)
Williams, J. P., Blitz, L., & McKee, C. F. 1999, in Protostars and Planets IV, ed. V. Mannings, A. Boss, & S. Russell (University of Arizona Press), in press
Wiseman, J. J., & Ho, P. T. P. 1996, Nature, 382, 139
Wiseman, J. J., & Ho, P. T. P. 1998, ApJ, 502, 676
Wolniewicz, L., Sibotin, I., & Dalgarno, A. 1998, ApJS, 115, 293
Yates, J. A., Field, D., & Gray, M. D. 1997, MNRAS, 285, 303